High temperature evolution of interfacial metal film bonding two 4H-SiC substrates

Maëlle Le Cunff, François Rieutord, Didier Landru, Oleg Kononchuk, Nikolay Cherkashin

Applied Surface Science 682 (2025) 161678

Contents lists available at ScienceDirect

Applied Surface Science

journal homepage: www.elsevier.com/locate/apsusc

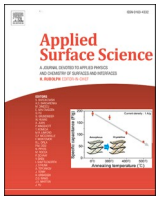

Full Length Article

High temperature evolution of interfacial metal film bonding two 4H-SiC substrates

Maëlle Le Cunff [a,b], François Rieutord [a], Didier Landru [a], Oleg Kononchuk [a], Nikolay Cherkashin [b,*]

[a] Innovation, SOITEC, Parc Technologique des Fontaines, Chemin des Franques, 38190 Bernin, France
[b] CEMES-CNRS and Université de Toulouse, 29 Rue Jeanne Marvig, BP 94347, 31055 Toulouse Cedex 4, France

ARTICLE INFO

Keywords:
4H-SiC
Metals
MAX phase
Wafer bonding
Wetting
AbStrain

ABSTRACT

The high temperature behavior of thin metal films (tungsten and titanium) confined between two off-axis single crystal SiC substrates is investigated. Through the application of transmission and scanning transmission electron microscopy, scanning electron microscopy, and X-ray scattering techniques, we examine the phase and morphology changes induced by high temperature annealing in thin layers consisting of these materials, as well as at their interfaces with SiC. Upon high-temperature annealing, a uniform and continuous W film formed by low-temperature deposition undergoes a transition to an array of discontinuous domains surrounded by a direct SiC/SiC interface. In contrast, a Ti film remains continuous with a strong thickness alteration. In parallel to step-bunching process of the internal SiC surfaces, both materials transform into new crystalline phases which contain Si and/or C atoms and achieve an epitaxial relationship with the SiC structures. The experimental findings are discussed in terms of dewetting phenomena and analyzed in light of potential chemical and structural reactions that may occur during interface reconstructions.

1. Introduction

Silicon carbide's large band gap and high thermal conductivity make it a popular material for power electronics [1,2]. Especially interesting for use in electronics devices is the stacking of thin SiC layers of high quality over a substrate with varying doping levels and quality via wafer bonding [3–5]. A layer of intermediate material acting as a glue can be utilized to provide a strong binding between a SiC layer and a SiC substrate, as direct SiC/SiC bonding may prove challenging due to the formation of an isolating and low adhesive layer at the interface [6]. The fabrication of power devices at high temperatures necessitates a thorough investigation of the evolution of these bonding layers under such conditions.

When selecting a material for the bonding layer, some applications, e.g., Vertical Diffusion Metal-Oxide Semiconductor (VDMOS) transistors [7] require conductive SiC/layer/SiC interface. While bonding with a SiO_2 layer has been demonstrated for insulating substrate manufacturing (SiCOI) and extensively studied in the literature [8–11], it is incompatible with such a specific requirement. The use of a semiconductor Si layer as a bonding layer is possible and the behavior has been extensively studied [12]. At high enough temperature, the Si layer breaks into isolated inclusions surrounded by direct SiC/SiC contacts. The Si dewetting from the SiC internal surfaces at temperatures below the Si melting point and a strong interface reconstruction at higher temperatures, over the Si melting point, are found to be responsible for the formation of such a structure. However, without changing its phase, Si inclusions present a potential barrier for conduction at the interface [13].

Titanium and tungsten, both conductive materials, represent valuable alternatives for SiC/SiC conductive bonding. In this work, we address the structural and compositional changes in nanometer-thick amorphous layers of titanium (Ti) and tungsten (W) sandwiched between two single crystalline SiC substrates, which were exposed to high-temperature annealing above and/or below their respective melting points. Specifically, we examine the impact of the annealing temperature, the initial deposition thickness and the formation of novel conductive crystalline phases. The purpose of this work is to provide an insight on the fundamental changes within a thin metallic layer confined

* Corresponding author.
E-mail addresses: maelle.le-cunff@soitec.com (M. Le Cunff), francois.rieutord@soitec.com (F. Rieutord), didier.landru@soitec.com (D. Landru), oleg.kononchuk@soitec.com (O. Kononchuk), nikolay.cherkashin@cemes.fr (N. Cherkashin).

https://doi.org/10.1016/j.apsusc.2024.161678
Received 17 September 2024; Received in revised form 22 October 2024; Accepted 30 October 2024
Available online 6 November 2024

between single crystal SiC structures under high temperature annealing in order to evaluate its potential use for a conductive wafer −to- wafer bonding.

2. Experiments

We utilized two 4H-SiC off-axis single crystal wafers with the [0001] (Si-terminated) and the [000$\bar{1}$] (C-terminated) axes rotated by 4° around the in-plane [1$\bar{1}$00] direction away from the normal to the wafer surface. Prior to bonding, the C-face SiC substrate was implanted with H^+ ions. A process called atomic diffusion bonding (ADB) (developed by T. Shimatsu and U. Uomoto) was used to prepare the SiC/SiC stacked samples [14–17]. This method, conducted at room temperature, involves sputter deposition of thin films onto two wafers, followed by the direct vacuum bonding of the two substrates. Thin layers of W or Ti were deposited onto both SiC substrates. Then, maintaining the coaxial alignment of crystallographic directions, the SiC substrates were bonded under high vacuum conditions, bringing into contact the two surfaces of W or Ti. It is worth noting that the bonding layer comes into contact with the Si-face and C-face SiC surfaces from different sides, resulting in two distinct SiC/metal interfaces. After bonding, the stacked wafers were annealed in a range of temperatures of 900 °C-1000 °C allowing the transfer of a thin SiC layer on top of the Si-face SiC substrate. This SmartCut™ process was used to create a 800 nm-thick SiC layer. The SiC/film/SiC structures were cleaved into pieces and heated to different temperatures, below the melting point of W (3422 °C [18]) and below and above the melting point of Ti (1668 °C [19]), during a second annealing cycle.

After bonding, scanning electron microscopy (SEM) and AFM were performed to examine the W and Ti thin films' upper surface after the thin SiC layers were removed via cleavage. The cross-sectional transmission electron microscopy (TEM) techniques were utilized to characterize the structure and morphology of interfaces, ascertain the crystalline phases present in the layers, and analyze their crystallographic orientation with respect to SiC. The images were performed using the aberration corrected SACTEM-Toulouse (Tecnai-FEI) and conventional Jeol2010 microscopes operating at 200 kV. High-resolution high angle annular dark-field scanning transmission electron microscopy (HR-HAADF-STEM) images were used for visualizing heavy atoms of the structures. The images were acquired at probe corrected JEOL JEM ARM 200F operating at 200 kV. The Abstrain procedure and correspondent plug-ins for Gatan Digital Micrograph [20] were utilized to rectify the image distortions and calibration errors. From those corrected images, crystalline phases were identified and strain with reference to the Bravais lattices of the correspondent structures were quantified. Thin TEM lamellas were prepared following the lift-out procedure and using the FEI Helios Nanolab 600i focused ion beam (FIB) operating between 30 kV and 2 kV. X-ray diffraction (XRD) measurements were performed to identify the crystalline phases at a macroscopic scale and evaluate the film textures. Those experiments were realized with laboratory equipment using copper or cobalt sources.

3. Results

3.1. Tungsten bonding

In this section, we investigate structures bonded with thin W layers. The samples were prepared with an as-deposited film thickness of 1 nm to 4 nm, followed by exposure to high annealing temperatures ranging from 1700 °C to 1900 °C, still far below the melting point of 3422 °C of W.

Fig. 1 shows the results of SEM, STEM and TEM investigation of the SiC/2 nm-thick W/SiC structure annealed at 1900 °C for 30 min.

The 52°-tilted SEM image of this structure following the removal of the top SiC layer reveals the presence of dark-contrast spots which are

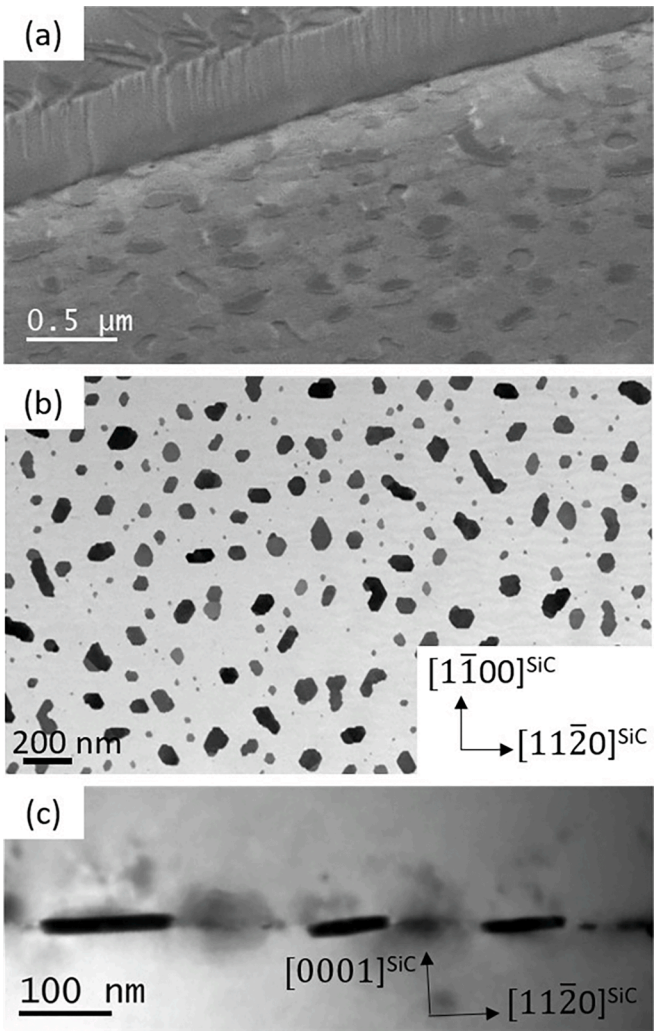

Fig. 1. SEM, STEM and TEM images of the SiC/2 nm W/SiC structure annealed at 1900 °C for 30 min: (a) 52°-tilted SEM image of the interface once the top substrate has been removed by cleavage; (b) Bright-field plan view STEM image; (c) Bright-field cross-sectional (1$\bar{1}$00) TEM image of the nodules.

likely to be attributed to W-containing inclusions (Fig. 1(a)). The transformation of initially continuous amorphous W layer into isolated crystalline inclusions is confirmed both by bright-field STEM plan-view (Fig. 1(b)) and cross-sectional (1$\bar{1}$00) (Fig. 1(c)) imaging. No voids are detected within the structure. The surface fraction S_f of the nodules is measured at 17 %. The rest 83 % of the surface is occupied by a direct SiC/SiC interface (Fig. 1(b) and (c)). The TEM image shows the existence of steps at SiC inner surfaces around the inclusions. The upper and bottom surfaces of the nodules are parallel to (0001) SiC. Both TEM plan view and cross-sectional images indicate that the inclusions have a quasi-cylindrical shape with facetted borders. Some inclusions reveal an irregular shape most likely due to a coalescence phenomenon. The inclusions have a density of 44 μm^{-2} and a lateral size which varies between 40 nm and 150 nm. The inclusions have the same thickness h of 14 nm, independent of their lateral size.

By using the geometrical parameters of the inclusions and the atomic density of W within the as-deposited layer of $\rho_W^l = 6.3 \times 10^{22} cm^{-3}$ (2 atoms per unit cell of pure W) [21], we estimate the concentration of W atoms within the inclusions as $\rho_W^{incl} = \rho_W^l \frac{h_0}{S_f h} = 5.29 \times 10^{22} cm^{-3}$. Such a value is 1.19 times less than that of pure W. This indicates a different from pure W composition within the nodules. Further on, we confirm such a finding through the determination of their structure with two

different approaches by measuring the interplanar distances and angles over their TEM images.

The first method is based on AbStrain analysis [20] of the cross-sectional $(11\bar{2}0)$ (Fig. 2(a)) and $(1\bar{1}00)$ (Fig. 3(a)) HR-TEM images of the nodules formed after annealing at 1800 °C for 30 min. The nodules were sectioned by a thin TEM lamella. Prior to a quantification treatment, the images were fully corrected from distortions and calibration errors by AbStrain procedure [20] by using separate images of 4H-SiC structure taken beneath (not shown).

The cross-sectional $(11\bar{2}0)$ image (Fig. 2(a), see insert on the left) and the Fast Fourier Transform (FFT) of the zone of the nodule (Fig. 2(b)) indicate that the nodule possesses a single crystal structure, with the crystalline planes aligned with that of the SiC substrate. It indicates an epitaxial relation between the nodule and the SiC substrate structures. The interface between the bottom and the upper SiC structures (see its zoomed part in the right insert) contains a stacking fault. Such a stacking fault suggests that the creation of an interim thin layer of the 3C-SiC structure occurs during the transition from one 4H-SiC structure to the other.

Fig. 2(b) shows the FFT of the nodule's region of the image with the horizontal and vertical reciprocal vectors $\mathbf{g_1}$ and $\mathbf{g_2}$ used for the AbStrain analysis. Fig. 2 (c–e) shows the maps of the corresponding interplanar distances and the angle between these reciprocal vectors. The average values of 2.585 ± 0.005 Å for d_1 and of 2.365 ± 0.005 Å for d_2 are measured within the nodule and indicated over the images. The measurements in the SiC image region closely match the values of the 4H-SiC structure, which indicates a high accuracy of the image correction. An angle of 90 ± 0.2° is measured between the correspondent reciprocal vectors. The reciprocal vectors are found to be collinear with that of the 4H-SiC structure indicating likely a hexagonal structure in the nodule. By making such an assumption, the lattice parameters are found to be of a = 2.985 Å and c = 4.730 Å. These values are in good agreement with the lattice parameters of the W_2C phase (space group P-31 m 164, a^{W_2C}=2.99 Å, c^{W_2C}=4.73 Å [22]) which gives $d^{W_2C}_{1\bar{1}00} = 2.59$ Å and $d^{W_2C}_{0002} = 2.365$ Å.

The maps of the strain tensor and rigid body rotation components extracted with reference to the Bravais lattice of W_2C are shown in Fig. 2 (f–i). Since all the average values of the strain tensor components are within ± 0.1 %, the nodule is indeed composed of the fully relaxed W_2C structure. The upper and the bottom SiC structures are clockwise and anticlockwise rotated by 0.5° close to the right apex of the nodule, respectively, as measured from the rigid body rotation map. The in-plane, shear and rigid body rotation maps clearly indicate the presence of the net of misfit dislocations all around the inclusion (see the arrows in Fig. 2(f) and the Bragg filtered image of one of the dislocations extracted from the displacement map). The inclined facets contain mixed type dislocations. At the (0001) nodule/SiC interfaces, the projection of the Burgers vector **b** in the image plane has only an in-plane component with a length of about 0.26 Å. The dislocations are separated by an average distance of 9 ± 2 nm. For a fully relaxed W_2C structure with an in −plane misfit of −2.95 % with the 4H-SiC structure, a distance of 8.6 nm is expected between the dislocations with such a Burgers vector, which corresponds well to the measured value.

To gain a three-dimensional view of the nodule's structure, the $(1\bar{1}00)^{SiC}$ projection of another nodule of the same structure has been analyzed. Fig. 3(a) shows the AbStrain corrected HR-TEM image of a

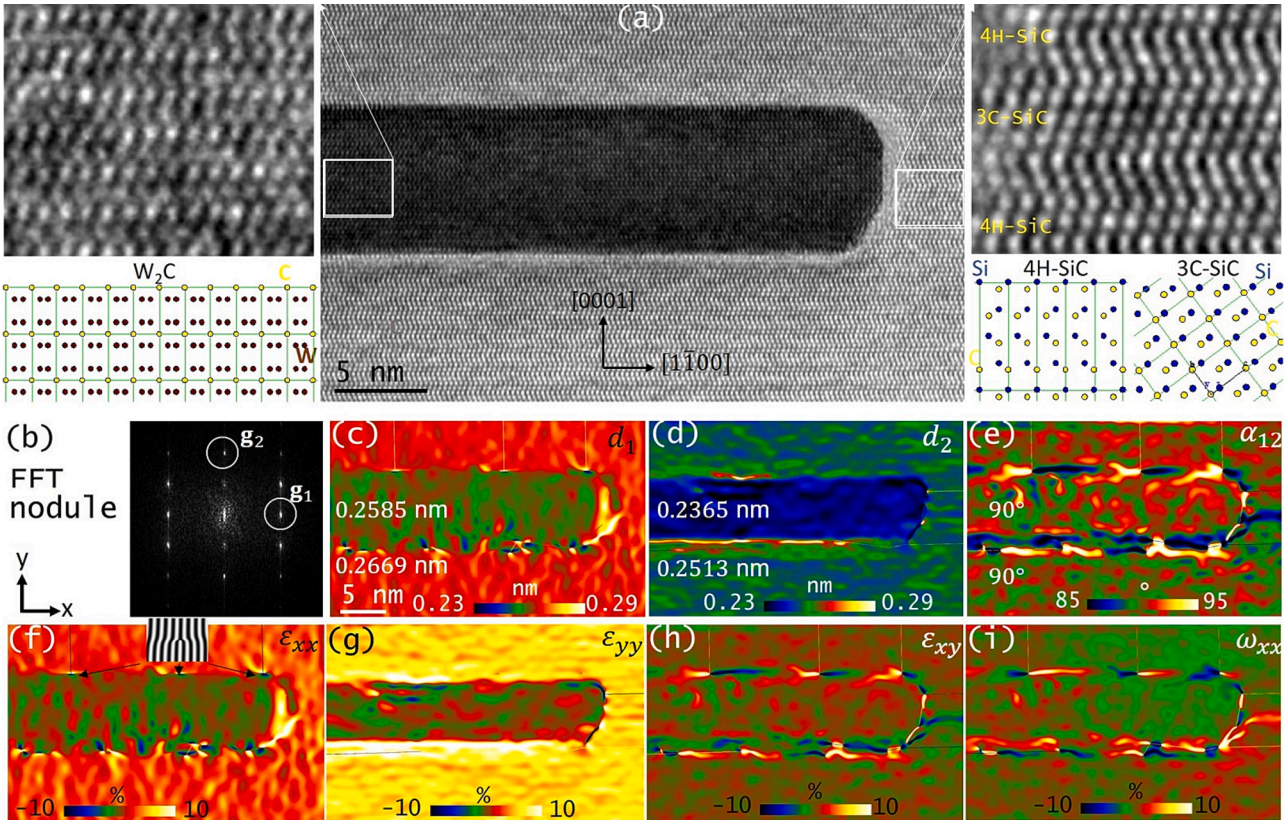

Fig. 2. AbStrain analysis (b–i) of the cross-sectional $(11\bar{2}0)$ HR-TEM image (a) of the W_2C nodule formed after annealing at 1800 °C for 30 min: (a) inserts on the left show the zoomed region of the nodule's image and corresponding hexagonal structure of W_2C. Inserts on the right show the zoomed region of the interface between the bottom and upper 4H-SiC structures which is mediated by the transition layer of the 3C-SiC structure; (b) FFT of the nodule's region of the image with the reciprocal vectors $\mathbf{g}_1$ and $\mathbf{g}_2$ used for the AbStrain analysis; (c–e) maps of the interplanar distances and the angle between $\mathbf{g}_1$ and $\mathbf{g}_2$. Numbers indicate the average values measured within the W_2C and SiC regions; (f–i) maps of the strain tensor components ε_{ij} and rigid body rotation ω_{ij} extracted with reference to the Bravais lattice of W_2C. Some misfit dislocations with the in-plane Burgers vector are indicated in (f) by arrows. The scale bar shown in (c) is valid for (c–i) figures.

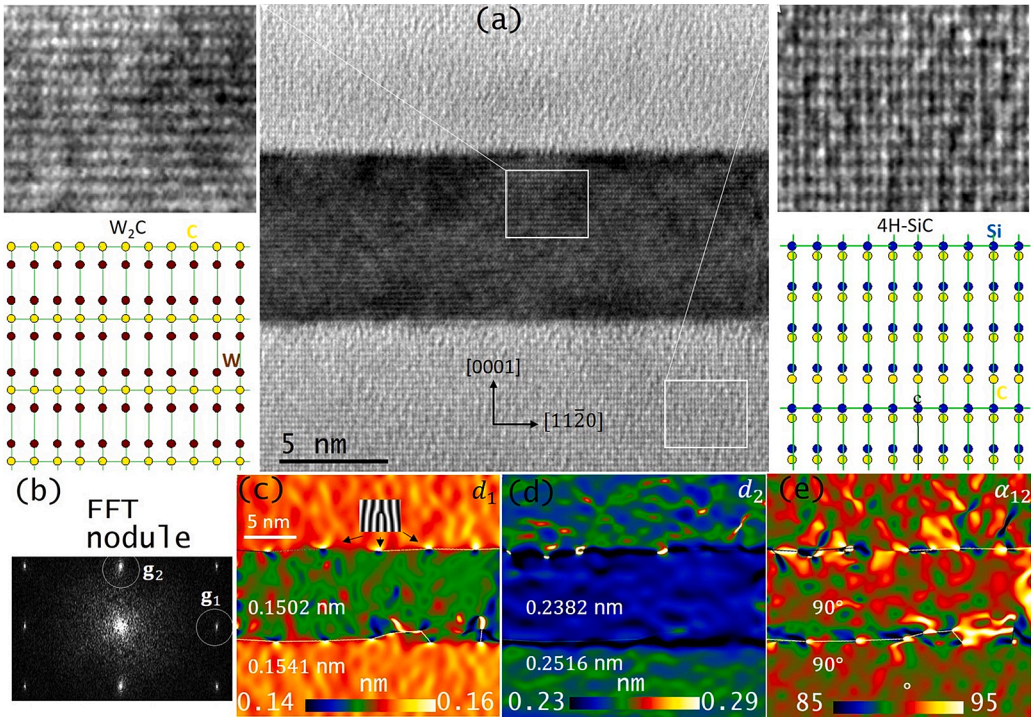

Fig. 3. AbStrain analysis (b–e) of the cross-sectional $(1\bar{1}00)$ HR-TEM image (a) of the W_2C nodule formed after annealing at 1800 °C for 30 min: (a) inserts on the left show the zoomed region of the nodule's image and corresponding hexagonal structure of W_2C. Inserts on the right show the zoomed region of the bottom 4H-SiC substrate and it's structure; (b) FFT of the nodule's region of the image with the reciprocal vectors $\mathbf{g}_1$ and $\mathbf{g}_2$ used for the AbStrain analysis; (c–e) maps of the interplanar distances and the angle between $\mathbf{g}_1$ and $\mathbf{g}_2$. Numbers indicate the average values measured within the W_2C and SiC regions. Some misfit dislocations with the in-plane Burgers vector are indicated in (c) by arrows. The scale bar shown in (c) is valid for (c–e) figures.

part of the nodule. Its zoomed region is shown in insert on the left side of Fig. 3(a). The analysis of its FFT (Fig. 3(b)) and comparison with the structure of SiC (see insert on the right side of Fig. 3(a)) confirm that the nodule is also seen along its $[1\bar{1}00]$ direction. The AbStrain analysis of its image (Fig. 3 (b-e)) provides the maps of the interplanar distances and the angle between the reciprocal vectors shown in Fig. 3(b).

The average values of 1.502 ± 0.005 Å for d_1 and of 2.382 ± 0.005 Å for d_2 are measured within the nodule and indicated over the images. These measurements correspond well to the nominal values $d^{W_2C}_{11\bar{2}0} = 1.50$ Å and $d^{W_2C}_{0002} = 2.37$ Å. The dislocations seen in Fig. 3(c) are separated by a distance of 4.8 nm. They have an in-plane component of the projected Burgers vector of a length of 1.5Å. With an in-plane misfit of -2.95 %, an expected distance between these dislocations in the W_2C structure fully relaxed on a 4H-SiC substrate is of about 5 nm, which corresponds well to the measured value of 4.8 nm.

All these findings confirm that the nodules obey the hexagonal W_2C structure (see the right-side inserts in Fig. 2(a) and Fig. 2(b)). The following crystallographic relationships are satisfied: $(0001)^{W_2C}//(0001)^{SiC}$, $\langle hk\overline{h+k}0\rangle^{W_2C}//\langle hk\overline{h+k}0\rangle^{SiC}$.

We have applied an alternative method for the analysis of the interplanar distances in the nodules formed after annealing at 1900 °C for 30 min. The method is based on the analysis of the moiré patterns formed over the dark-field and bright-field cross-sectional $(1\bar{1}00)$ images of the inclusion (Fig. 4 (a), (b)). Here, the nodule is embedded within a thick enough TEM lamella that ensured its coating by the SiC structure. The images are taken at two beam conditions with $\mathbf{g} = 11\bar{2}0$ (Fig. 4 (a)) and $\mathbf{g} = \bar{1}\bar{1}24$ (Fig. 4 (b)).

The moiré patterns appear due to the interference of the waves diffracted from the $(11\bar{2}0)$ or $(\bar{1}\bar{1}24)$ SiC planes with that of the inclusion's structure. Each image prominently exhibits a one-fringe family pattern, characterized by a distinct period and inclination. Such a moiré pattern can serve for the determination of the interplanar distances of the

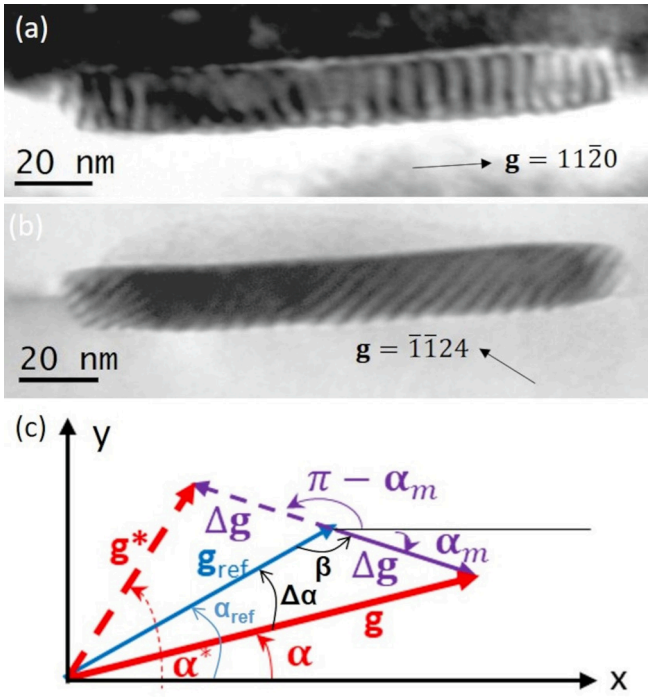

Fig. 4. (a), (b) Cross-sectional $(1\bar{1}00)$ TEM images of the nodule formed after annealing at 1900 °C for 30 min: (a)dark-field image taken with g = 11$\bar{2}$0; (b) bright-field image taken with g = $\bar{1}\bar{1}$24; (c) Schematic representation of the single fringe moiré pattern in the reciprocal space. Blue, red and violet colors indicate reference, unknown and moiré structures, respectively. Solid and dashed lines represent the same moiré fringe pattern which can be formed with different structures.

unknown structure and of its misorientation with the matrix structure with a high precision [23]. Let's consider $\mathbf{g}_{ref}$ and $\mathbf{g}$ to be the diffraction vectors of the reference lattice and the unknown structure, respectively (Fig. 4(c)). $\Delta\mathbf{g}$ is defined as $\Delta\mathbf{g} = \mathbf{g} - \mathbf{g}_{ref}$. Its direction is perpendicular to the moiré fringes making an angle α_m with the horizontal axis and its length is in inverse proportion to their period T given by $|\Delta\mathbf{g}| = \frac{1}{T}$. The period T and α_m can be measured from the TEM images (Fig. 4(a) and (b)). However, the position of the diffraction spot of the unknown structure must be identified from the corresponding diffraction pattern since α_m or $\pi - \alpha_m$ result in the same moiré period while provide different g (see $g*$ in Fig. 4(c), dashed lines). The angle β between $\Delta\mathbf{g}$ and $\mathbf{g}_{ref}$ is calculated using the values of α_m and the angle α_{ref} between $\mathbf{g}_{ref}$ and the horizontal axis. α_{ref} is measured from the corresponding diffraction pattern. $|\mathbf{g}_{ref}|$ is in inverse proportion to the $\{hkl\}^{SiC}$ interplanar distance d_{ref}. From a simple geometrical consideration, the interplanar distance d in the unknown structure and the angle $\Delta\alpha$ between $\mathbf{g}_{ref}$ and $\mathbf{g}$ can be calculated as

$$\begin{cases} d = \dfrac{1}{\sqrt{\left(\dfrac{1}{d_{ref}^2} + \dfrac{1}{T^2} - \dfrac{2}{Td_{ref}}\cos\beta\right)}}, \\ \Delta\alpha = \cos^{-1}\left(\left(\dfrac{1}{d^2} + \dfrac{1}{d_{ref}^2} - \dfrac{1}{T^2}\right)\dfrac{dd_{ref}}{2}\right). \end{cases} \quad (1)$$

By measuring T and β for two different $\mathbf{g}_{ref}$ and substituting these values in Eq. (1), we calculated the interplanar distances as well as the corresponding angles between $\mathbf{g}_{ref}$ and $\mathbf{g}$ for the unknown structure. For $\mathbf{g}_{ref}=11\bar{2}0$, the average fringe period is measured of 5.3±0.5 nm and the average angle β of 179.9±0.5°. By substituting these values and $d^{SiC}_{11\bar{2}0} = 0.1541$ nm for d_{ref} in Eq. (1), we get $d_1 = 0.15 \pm 0.005$ nm and $\Delta\alpha_1 \cong 0^\circ$. For $\mathbf{g}=\bar{1}\bar{1}24$, the average fringe period is measured of 3.8±0.5 nm and the average angle β of 179.5±0.5°. With $d_{ref} = d^{SiC}_{\bar{1}\bar{1}24} = 0.1314$ nm we get $d_2 = 0.127 \pm 0.005$ nm and $\Delta\alpha_2 \cong 0^\circ$. The angle between $\mathbf{g}_1$ and $\mathbf{g}_2$ is calculated of 32 ±0.5°. By presuming that the inclusion has the hexagonal structure we index $\mathbf{g}_1 = 11\bar{2}0$ and $\mathbf{g}_2 = \bar{1}\bar{1}22$ and obtain a=3.0 ± 0.05 Å, c=4.77 ± 0.05Å which corresponds to the hexagonal structure of the W_2C nodules formed after annealing at 1800 °C.

Finally, we performed macroscopic-scale X-ray diffraction measurements in order to determine average structural characteristics of the population of inclusions. Fig. 5(a) shows the θ/2θ scan aligned on the $(0004)^{SiC}$ planes. A cobalt source with a wavelength λ of 1.789 Å was used for this experiment.

The curve presents two peaks at 2θ = 41.5° and 2θ = 44.46° which correspond to d_{hkl} = 2.52 Å and d_{hkl} = 2.36 Å, respectively. The first peak is referent to the (0004) reflection of 4H-SiC. The second peak corresponds well to the reflection of the (0002) W_2C planes. Fig. 5(c) shows that the full width at half maximum increases as the film thickness decreases, with values of 1.4°, 1° and 0.51° for the thicknesses of 1 nm, 2 nm and 4 nm, respectively. That allows the estimation of the average nodule thickness which changes from 10 nm in a 1 nm-thick W film to 15 nm and 28 nm in 2 nm and 4 nm-thick W films, respectively.

Fig. 5(b) shows the reciprocal space mapping over these reflections in a 4 nm-thick W film. The reflection of the (0002) W_2C planes is perfectly aligned with that of the (0004) SiC planes in the $[0001]^{SiC}$ direction. Thus, W_2C hexagonal nodules are single crystalline with an epitaxial relationship with the SiC substrates.

The interplanar distances and angles within the inclusions' crystal were measured both locally and macroscopically, allowing for their attribution to the W_2C hexagonal structure. From this result, we can estimate the quantity of W and C contained within the population of inclusions, compare these values with the amount of W available in the as-deposited W layer and estimate the thickness of a SiC layer which was

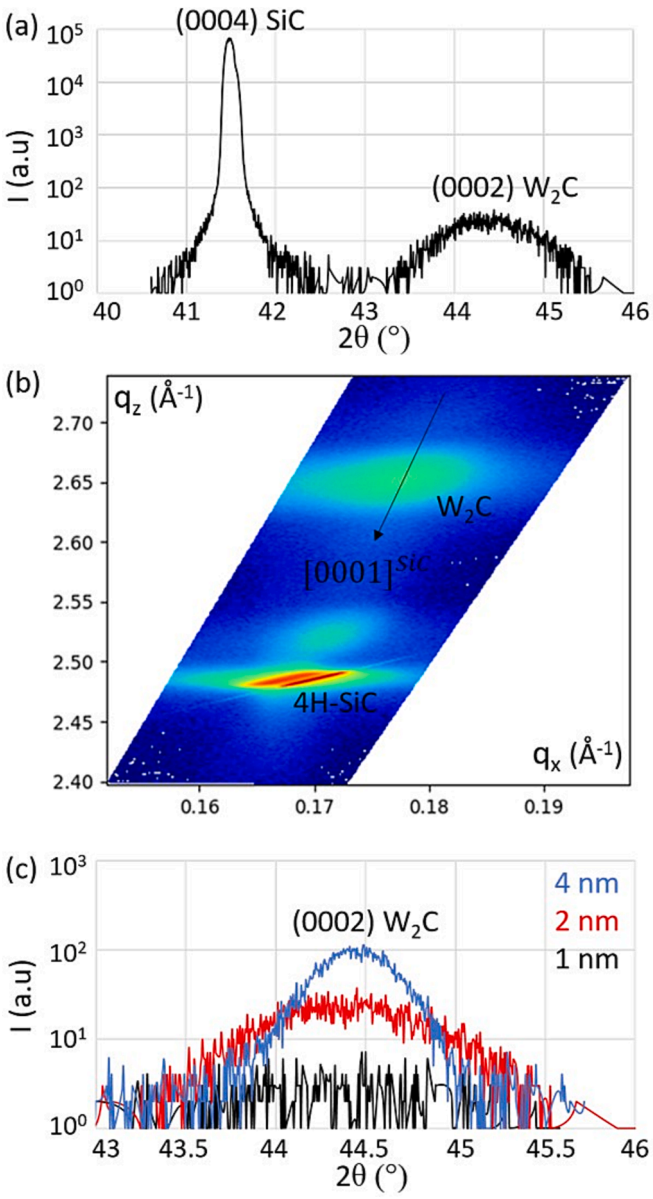

Fig. 5. X-ray diffraction data from the W films annealed at 1900 °C for 30 min: (a) θ/2θ diffraction scan along the $[0001]^{SiC}$ direction for a 2 nm-thick W film; (b) Reciprocal space mapping around the (0004) SiC planes for a 4 nm-thick W film; (c) θ/2θ diffraction scan along the $[0001]^{SiC}$ direction for three different film thickness.

dissolved during annealing from both SiC surfaces.

The unit cell of W_2C contains 6 W atoms and 3C atoms which provides an atomic density of W atoms of 5.44×10^{22} cm^{-3}. It is 1.16 times less than the atomic density of W atoms in pure W. Such a value corresponds well to our previous estimation of a factor of 1.19 calculated from the volume per surface fraction occupied by 14 nm-thick nodules formed in a 2 nm-thick W layer after annealing at 1900 °C for 30 min (Fig. 1).

The atomic density of C atoms within W_2C structure is of 2.72×10^{22} cm^{-3}. The surface density of C atoms contained within the 14 nm-thick nodules occupying 0.17 of the surface is thus calculated to 6.47×10^{15} cm^{-2}. The SiC substrate and the SiC layer are the only source of carbon atoms. Each unit cell of 4H-SiC contains 4C atoms that corresponds to 4.85×10^{22} cm^{-3} density of C atoms. By dividing the surface density of C atoms contained within the nodules by this value, we estimate a thickness of the dissolved SiC layer of 1.33 nm, i.e., about 5 to 6 (0004) planes

of 4H-SiC has been dissolved in total from the internal surfaces of the SiC substrate and the transferred layer.

In parallel, the surface density of Si atoms released by SiC dissolution must be equal to that of C atoms. For an atomic density of fcc Si of 5×10^{22} cm^{-3}, the thickness of released Si per surface fraction of dissolved SiC layer is of 1.3 nm. It was difficult to find such a little amount using the current techniques, which may be dispersed as thin shells surrounding the W_2C nodules or as isolated Si nodules in a weak density.

To conclude, from this part of the experiments, we learned that the homogeneous W film fragments into nodules after annealing at high temperature. The nodules are surrounded by a direct 4H-SiC/3C-SiC/4H-SiC interface. The nodules have hexagonal W_2C phase structure which has an epitaxial relation with the SiC substrates. The nodules are completely plastically relaxed by the formation of the net of misfit dislocations at their interface with the SiC structure. Dissolution of several (0004) planes at SiC inner surfaces provided enough carbon to justify such a phase transformation.

3.2. Titanium bonding

In this part, we studied the SiC/10 nm-thick Ti/SiC bonded structures annealed at temperatures below and above the Ti melting point of 1668 °C.

3.2.1. Below Ti melting point

First, we studied the sample annealed at 1550 °C for 30 min. Fig. 6(a) shows the SEM image of this structure after cleaving out the top layer. The light spots distributed over the darker background indicate the presence of nodules within a continuous Ti-containing layer. No voids are observed.

Fig. 6(b) shows the bright-field cross-sectional $(1\bar{1}00)^{SiC}$ TEM image of this sample. Small steps and large terraces together with the step bunching are formed at both SiC internal surfaces. The bonding layer remains continuous but the thickness of this layer varies with the step height. When the steps are shallow of a height of 1–2 nm, the layer remains thin with a thickness of 10 nm. When the steps are of about 20 nm high, the layer thickness is doubled. This results in the formation of 50 nm- large nodules. Interesting to note that the nodules and the layer in-between have different structures as revealed by the corresponding diffraction patterns (Fig. 6(c) and (d)). As a common feature, both structures seem to get an epitaxial and pseudomorphic relationship with the SiC substrates.

By analyzing the length and the orientation of the selected diffraction vectors $\mathbf{g}_1$, $\mathbf{g}_2$, $\mathbf{g}_3$ (see white arrows in Fig. 6(c) and (d)), we deduced the corresponding interplanar distances in the nodule: $d_1 = 6.7 \pm 0.05$ Å, $d_2 = 2.5 \pm 0.05$ Å and $d_3 = 2.5 \pm 0.05$ Å and the angles 89° between the directions $\mathbf{g}_1$ and $\mathbf{g}_3$ and 70° between $\mathbf{g}_1$ and $\mathbf{g}_2$. Regarding the thin layer, we found $d_1 = 8.5 \pm 0.05$ Å, $d_2 = 1.5 \pm 0.05$ Å and $d_3 = 1.5 \pm 0.05$ Å and the angles 90° between the directions $\mathbf{g}_1$ and $\mathbf{g}_3$ and 80° between $\mathbf{g}_1$ and $\mathbf{g}_2$. Since Ti has crystallized at high temperatures, one would expect the formation of the hexagonal structure of alpha titanium with a = 2.951 Å et c = 4.681 Å [24]. However, neither of its interplanar distances corresponds to the experimentally obtained values. Thus, the chemical interactions between titanium and SiC structures have led to the creation of two new distinct crystalline phases, which will be determined later on.

3.2.2. Above Ti melting point

Here, we studied the structure annealed at 1700 °C, i.e above the melting point of Ti, for 30 min. Fig. 7(a) shows the SEM image of this structure which reveals contrast variation corresponding to the thin layer and presumably, to thick nodules. Distinct steps are clearly identifiable on top of the layer, indicating a significant interface reconstruction of SiC surfaces through step bunching at such a high temperature.

The cross-sectional $(1\bar{1}00)^{SiC}$ TEM image (Fig. 7(b)) indicates an increase in the height of the steps which is measured to be of 50 nm. In turn, the nodules also exhibit an increased thickness, with an average height of about 40 nm. It is noteworthy that the nodules are confined between the steps of both SiC internal surfaces and surrounded by a thin layer.

The diffraction patterns obtained for the thin layer and the nodule (Fig. 7(c) and (d)) are identical to those observed after annealing at 1550 °C (Fig. 6(c) and (d)) indicating the same correspondent structures. Additional investigations were conducted to identify their crystalline structures.

Fig. 8(a) shows the cross-sectional $(1\bar{1}00)$ HR-HAADF-STEM image of the thin layer.

This image is obtained as a result of the alignment and summing-up of a stack of 10 images each of which has been corrected for STEM induced distortions and calibration errors by applying Abstrain procedure [20]. The heavier element, titanium, is represented by the bright contrast spots in the image, whereas silicon is represented by the darker ones. Carbon atoms are too light to be discerned in such an imaging mode. SiC structure is represented at the bottom and the top parts of the image. It is clear that the thin layer is composed of two crystalline phases.

In the bottom part of the layer, there is a noticeable periodicity in the contrast of the atomic rows. The three high intensity layers, which are likely to represent Ti atoms, are alternated by a layer of a darker intensity, which is likely to represent Si atoms. Such a block of 4 layers is repeated in the $[0001]^{SiC}$ direction. From the left part of the intensity profile (Fig. 8(d)) extracted along the white arrow shown in Fig. 8(a), we can identify the periodicity of such a unit cell which is marked with the black rectangle. The mean distance between the Si fringes (low intensity peaks) is estimated of 8.7 Å and the mean distance between the Ti fringes (high intensity peaks) of 2.34 Å.

In the upper part of the layer, we see the periodic stacking of high

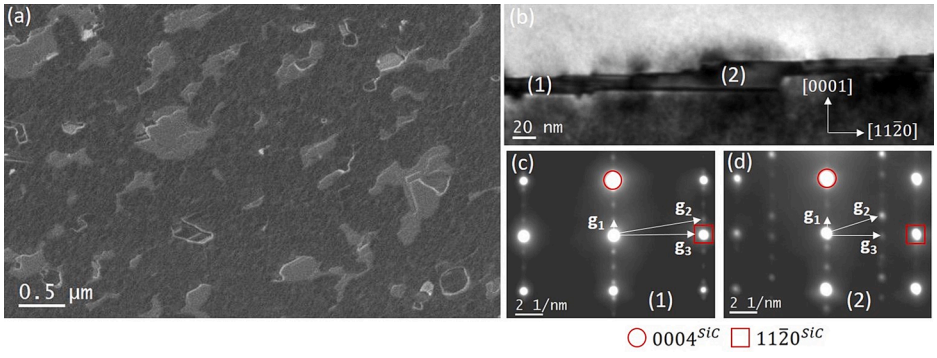

Fig. 6. A 10 nm-thick Ti layer annealed at 1550 °C for 30 min: (a) 52°-tilted SEM image once the top SiC layer has been removed by cleavage; (b) Bright-field $(1\bar{1}00)^{SiC}$ TEM image showing the thin layer (1) and the nodules (2); (c) Diffraction pattern from the thin layer; (d) Diffraction pattern from the nodule.

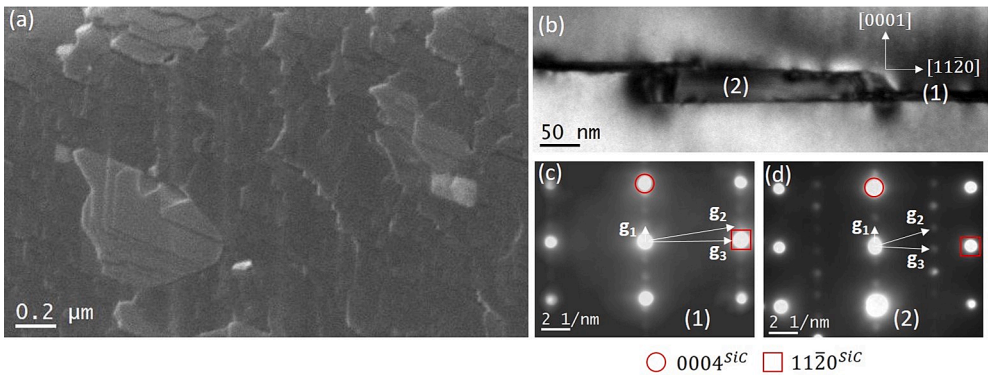

Fig. 7. A 10 nm-thick Ti layer annealed at 1700 °C for 30 min: (a) 52°-tilted SEM image once the top SiC layer has been removed by cleavage; (b) Bright-field $(1\bar{1}00)^{SiC}$ TEM image showing the thin layer (1) and the nodule (2); (c) Diffraction pattern from the thin layer; (d) Diffraction pattern from the nodule.

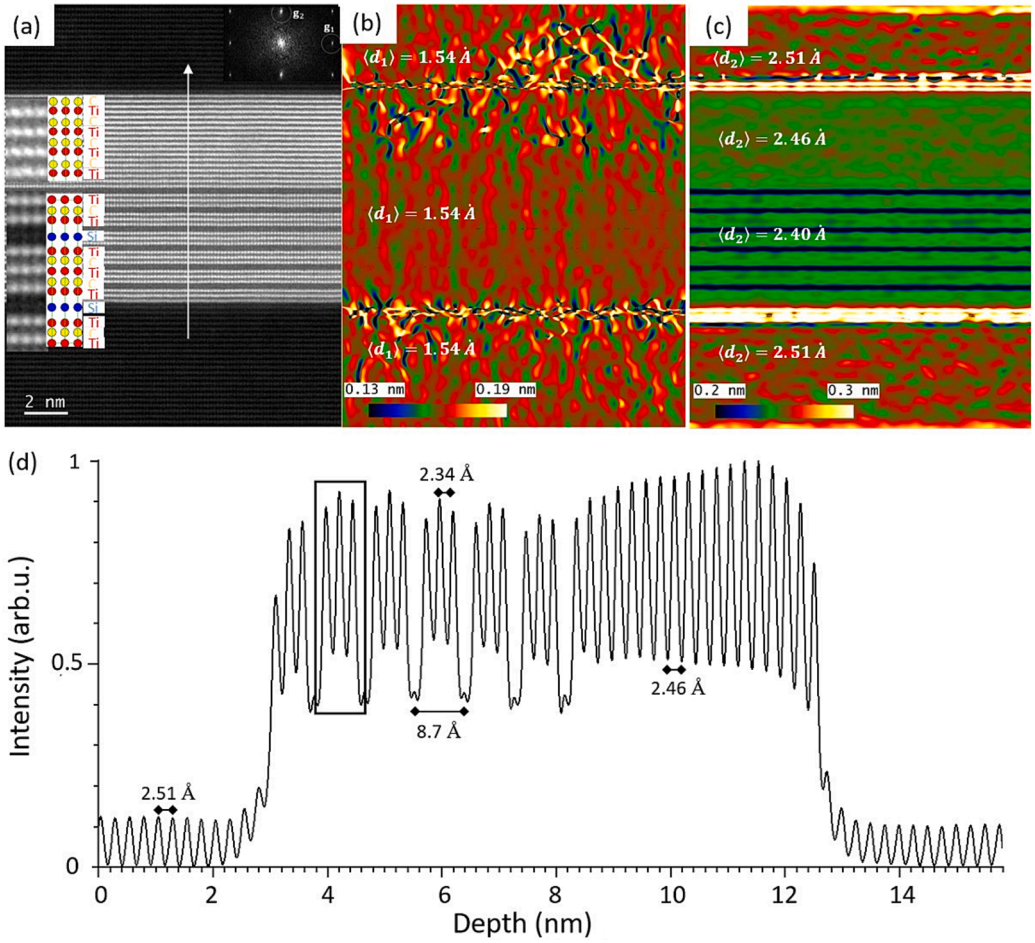

Fig. 8. A 10 nm-thick Ti layer annealed at 1700 °C for 30 min: (a) HAADF-STEM image of the thin layer. Insert shows FFT with $\mathbf{g}_1$ and $\mathbf{g}_2$ vectors selected for AbStrain analysis. AbStrain analysis of (a): (b), (c) maps of the interplanar distances corresponding to $\mathbf{g}_1$ (b) and $\mathbf{g}_2$ (c) in (a); (d) Intensity profile obtained in the $[0001]^{SiC}$ direction, see white arrow in (a).

intensity rows, which are likely to be represented by Ti atoms. From the right part of the intensity profile, the distance between the Ti planes is found to be of 2.46 Å.

We realized the quantitative measurement of the in-plane (Fig. 8(b)) and out-of-plane (Fig. 8(c)) interplanar distances in the layer by applying AbStrain analysis of the image. The identical color over the whole field of view in Fig. 8(b) implies the same in-plane interplanar distance throughout the stack. The similar average distance $\langle d_1 \rangle = 1.54\,\text{Å} \pm 0.01\,\text{Å}$ is measured at the various depths. Such a value corresponds to $d^{SiC}_{11\bar{2}0} = 1.541$ Å. It indicates that both layer phases are pseudomorphic to the SiC substrate. The map of the out-of-plane distance indicates that it changes from $\langle d_2 \rangle = 2.51 \pm 0.01$ Å in SiC to $\langle d_2 \rangle = 2.40 \pm 0.01$ Å in the three-layer blocks of the bottom layer phase then to $\langle d_2 \rangle = 2.46 \pm 0.01$ Å in the upper phase of the layer.

By combining all these data, the structure of the bottom layer phase can be attributed to the MAX phase of hexagonal Ti_3SiC_2 (space group P 63/mmc, a = 3.065 Å, c = 17.635 Å) [25] seen along the $[1\bar{1}00]^{MAX}$

direction. The upper part is likely to be composed of cubic TiC (space group F m-3 m, a = 4.325 Å) [26] seen along the $[1\bar{1}2]^{TiC}$ direction. The corresponding structures are shown in inserts of Fig. 8(a) where Ti, Si and C atoms are represented by red, blue and yellow solid circles, respectively.

The measured value of $\langle d_2 \rangle = 2.40 \pm 0.01$ Å for the MAX phase corresponds well to the distance of 2.38 Å which separates three sequent Ti layers lying on the (0008) planes of Ti_3SiC_2. The value of the in-plane interplanar distance $\langle d_1 \rangle = 1.54$ Å measured experimentally is also well consistent with $d_{11\bar{2}0}^{Ti_3SiC_2} = 1.537$ Å. The Ti_3SiC_2 layer is slightly in-plane tensile strained to a value of $\varepsilon_{xx} = \left(d_{11\bar{2}0}^{SiC} - d_{11\bar{2}0}^{Ti_3SiC_2}\right)/d_{11\bar{2}0}^{Ti_3SiC_2} = 0.2\,\%$.

For the upper part of the layer, the measured in-plane and out-of-plane interplanar distances fit well the $d_{220}^{TiC} = 2.531$ Å and $d_{111}^{TiC} = 2.50$ Å of the cubic TiC phase assuming it is tensile strained in the interface plane to a value of $\varepsilon_{xx} = \left(d_{11\bar{2}0}^{SiC} - d_{220}^{TiC}\right)/d_{220}^{TiC} = 0.7\,\%$. The measured out-of-plane interplanar distance of 2.46 Å is lower by −1.6 % than d_{111}^{TiC} due to the Poisson reaction.

The two structures identified in the thin layer, Ti_3SiC_2 and TiC, exhibit an epitaxial relation with the SiC substrates: $(0001)^{Ti3SiC2}$// $(0001)^{SiC}$, $<hk\bar{h}+\bar{k}0>^{Ti3SiC2}$// $<hk\bar{h}+\bar{k}0>^{SiC}$ and $(111)^{TiC}$// $(0001)^{SiC}$, $[110]^{TiC}$// $[11\bar{2}0]^{SiC}$, $[1\bar{1}2]^{TiC}$// $[1\bar{1}00]^{SiC}$.

The thick nodules obey different from the layer structure and composition. Fig. 9(a) shows the corrected HR-HAADF-STEM image of the bottom part of the nodule.

From the bottom, the layer starts with a (3 + 1) block of the MAX phase which is followed by the periodic blocks of two bright rows alternated by a darker row. Interesting to note that the intensity of the bright rows is lower while the intensity of the darker row is higher than that in the Ti and Si containing layers of the MAX phase, respectively. Such a finding suggests a mixture of Si and Ti atoms in these layers. The SiC and MAX phase structures' images clearly show both vertical and horizontal atomic planes, whereas the nodule's image does not. Only rows parallel to the $(0001)^{SiC}$ planes are resolved. That suggests either a twist misorientation of the layer structure with that of SiC or a much lower in-plane interplanar distance, that could not be resolved in the image. The periodicity of the rows is evidenced in the intensity profile (Fig. 9(c)) extracted along the white line shown in Fig. 9(a). The intensity profile provides an interplanar distance of 2.3 Å between two bright-contrast layer and of 6.7 Å between the (2 + 1) blocks. Alternatively, AbStrain analysis of the image was applied providing the map of the correspondent interplanar distance (Fig. 9(b)). An average value of $\langle d_2 \rangle = 2.20 \pm 0.01$ Å is measured within the part with the (2 + 1) periodicity.

While the structure of the thick nodule could not be identified unambiguously, we address the composition distribution there by applying EDX measurements (Fig. 10 (a-f)). Within the thick nodule, the absence of carbon within this structure is clearly revealed. The nodule contains twice more silicon than titanium which imposes a structure of $TiSi_2$ (space group C mcm, a = 3.61 Å, b = 13.77 Å, c = 3.65 Å [27]).

EDX measurements conducted in the bonding layer where the two distinct phases are observed (Fig. 10 (g)) confirm the presence of a phase rich in Ti, Si, and C at the bottom of the thin layer, where the MAX phase is identified, and a phase rich in Ti and C above with no signature of Si there, where TiC phase is identified (Fig. 10 (h)).

The macroscopic X-ray diffraction measurements in this structure are presented in Fig. 11. The θ/2θ scan aligned on the $(000l)^{SiC}$ planes reveals the presence of three sets of diffraction peaks. First, the peaks at 17.57°, 26.49°, 35.48°, 44.91°, 54.55° and 75.44° come from the diffraction of SiC crystalline planes: (0002), (0003), (0004), (0005), (0006) and (0008). The broader peaks observed at 10.08°, 20.06°, 30.35°, 40.83°, 51.72° and 88.45° exhibit a full width at half maximum (FWHM) of 1.15°, corresponding to a thickness of 7 nm. These peaks can be attributed to the diffraction from the 10 nm-thick thin layer (as extracted from TEM images). Those diffraction peaks are consistent with the Ti_3SiC_2 phase. They correspond respectively to the (0002), (0004), (0006), (0008), (00010) and (00016) crystalline planes. This finding can explain why the thickness measured from XRD experiments is lower than the total thickness of the thin layer observed at the interface. Only the diffraction from the Ti_3SiC_2 phase is observed; no peaks are identified for the TiC layer. The diffraction peak from the {111} TiC planes (2θ = 35.84°) is obscured by the diffraction from the (0004) SiC planes (2θ = 35.58°). The narrower peaks observed at 39.95° and 54.1° exhibit a full width at half maximum (FWHM) of 0.31°, corresponding to a thickness of 30.3 nm, which aligns well with the diffraction of the thick nodules. Such a value corresponds to the thickness of 37 nm measured in the TEM images. These peaks are consistent with the diffraction of {060} and {080} planes of the cubic $TiSi_2$ phase.

The θ/2θ scan in the out-plane direction $[11\bar{2}0]^{SiC}$ reveals the presence of several diffraction peaks. The peak at 60.032° corresponds to the diffraction of the $(11\bar{2}0)^{SiC}$ planes. The diffraction from the $(11\bar{2}0)$ Ti_3SiC_2 planes and {220} TiC planes is obscured by the diffraction from the SiC substrate. The additional peaks at 53.72°, 57.22°, 65.99° and 74.91° arise from the diffraction of the intermediate layer, specifically from the nodules. They are consistent with the diffraction of {220}, {112}, {260} and {222} $TiSi_2$ planes.

In conclusion, the as-deposited Ti layer evolves into three crystalline

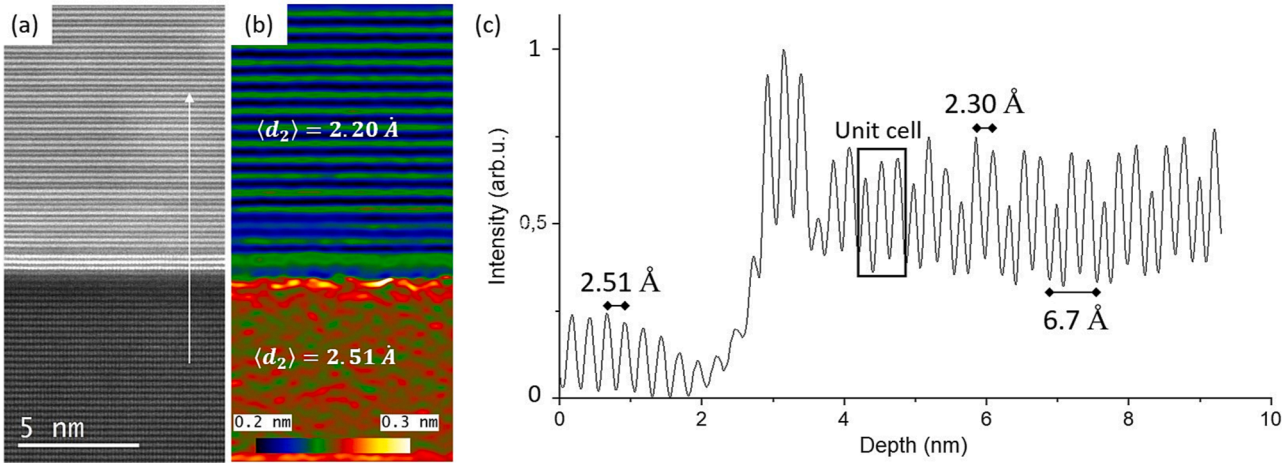

Fig. 9. A 10 nm-thick Ti layer annealed at 1700 °C for 30 min: (a) HAADF-STEM image of part of a thick nodule (top) and SiC substrate (bottom); AbStrain analysis of (a): (b) Map of the interplanar distance in the $[0001]^{SiC}$ direction; (c) Intensity profile obtained in the $[0001]^{SiC}$ direction, see white arrow in (a).

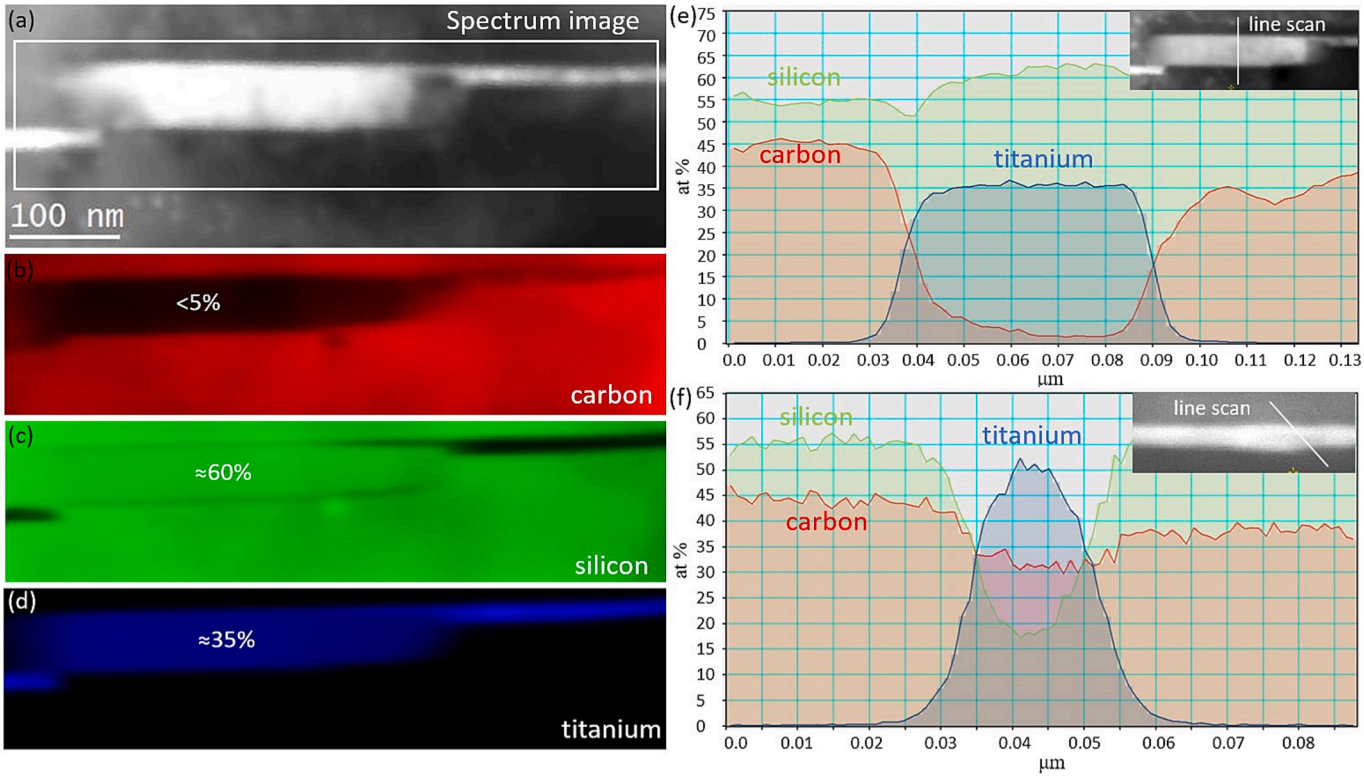

Fig. 10. A 10 nm-thick Ti layer annealed at 1700 °C for 30 min: (a) Low magnification HAADF-STEM cross-sectional $(1\bar{1}00)^{SiC}$ image of the interface; (b–d) EDX composition maps from (a): (b) C, (c) Si, (d) Ti; (e),(f) EDX line scan quantification in: (f) the thick nodule; (f) the thin layer. The scan directions are shown in inserts; (g) HAADF-STEM image of the thin layer with the regions of the EDX measurement; (h) EDX quantification results from (g).

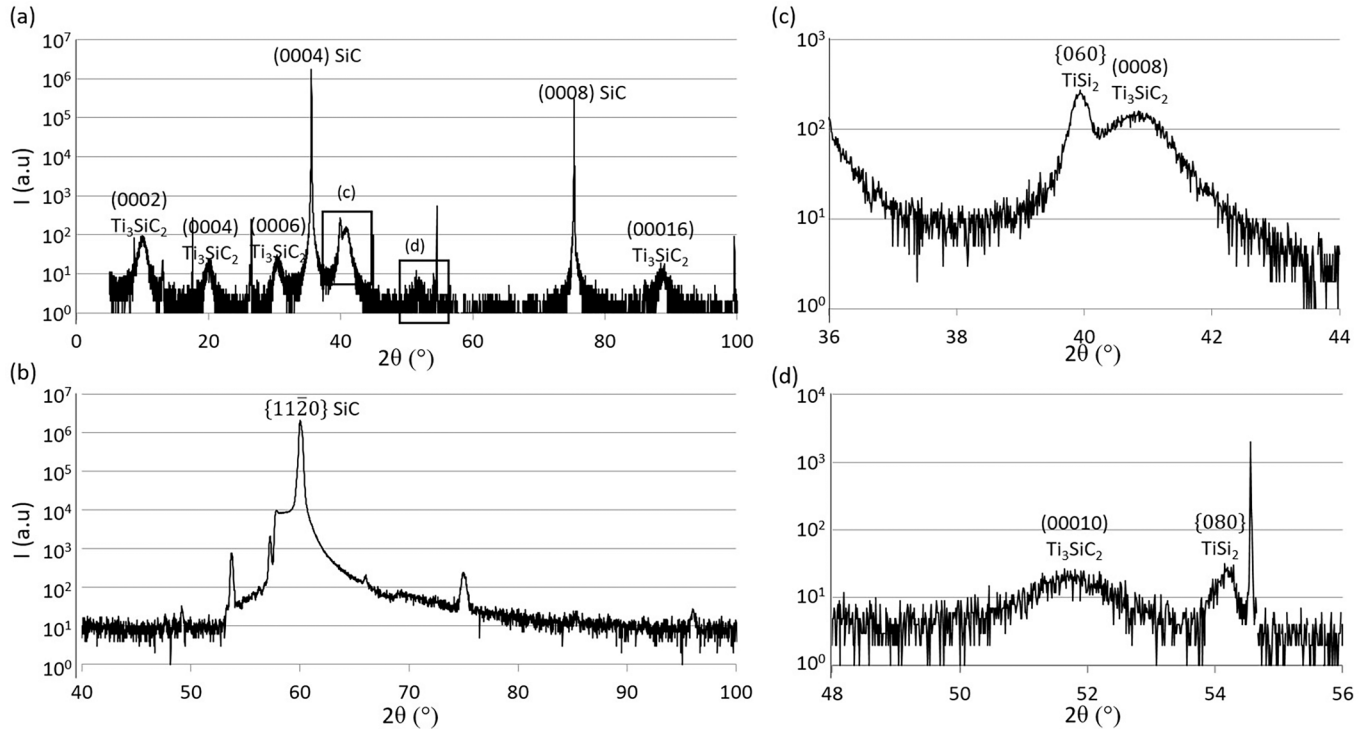

Fig. 11. A 10 nm-thick Ti layer annealed at 1700 °C for 30 min: (a) θ/2θ diffraction scan aligned in the $[0001]^{SiC}$ direction; (b) θ/2θ diffraction scan aligned in the $[11\bar{2}0]^{SiC}$ direction; (c) Zoom of the θ/2θ diffraction scan aligned in the direction [0001] for 2θ = 36°–44°; (d) Zoom of the θ/2θ diffraction scan aligned in the direction [0001] for 2θ = 48°–56°. Copper source (λ = 1.5404 Å).

phases. The thick quasi-isolated nodules contain an alloy of Si and Ti atoms in form of $TiSi_2$. The thin layer surrounding the nodules contain either an alloy of Ti, Si and C atoms in form of MAX phase of Ti_3SiC_2 or an alloy of Ti and C atoms in form of cubic TiC. The thin layer is pseudomorphic to the SiC substrate that imposes the presence of in-plane tensile stress there. On the contrary, the nodule structure seems to be fully relaxed.

4. Discussions

A solid-state fragmentation of the tungsten films together with the formation of a new crystalline phase in the individual nodules was shown. The contact angle between SiC and W_2C clusters can be estimated at $\sim$ 120° from the TEM cross-sectional images. Thus, the reduction of interfacial energy brought on by dewetting- that is, the decrease of the W/SiC contact surface- drives the fundamental process for W redistribution. The nodules have the W_2C hexagonal structure in an epitaxial relation with SiC substrates which is relaxed by misfit dislocations. From the phase diagrams of the W-C system proposed in the literature [28,29], W_2C is a stable phase obtained at high temperatures ($T > 1500$ °C) and for a small amount of carbon. The formation of W_2C hexagonal phase in our system is therefore in good accordance with thermodynamics and several authors have mentioned the formation of W_2C on SiC substrates at high temperatures [30–35]. The W_2C phase appears due to a chemical reaction occurring between tungsten and SiC surfaces. The formation of carbide phases is promoted by the dissolution of several (0004) planes of the internal surfaces of the SiC structures, which releases C atoms. The equivalent amount of silicon is likely to be embedded within the thin shells surrounding the nodules as TEM and EDX measurements do not reveal the presence of silicon-rich clusters. The amplified dissolution of SiC in the presence of a W layer is enabled by the low binding energy of Si, C atoms at the SiC/W interface compared to the SiC/vacuum interface. The solubility of carbon in tungsten is very low (≈0.3 at.%) [36]. However, as there is a strong concentration gradient of Si and C at this interface, Si and C atoms do diffuse in the layer reaching high enough concentrations, resulting in the formation of new W-Si-C alloy and the reconstruction of SiC internal surfaces. The system prefers to create structures during crystallization that cost less energy. According to the misfit analysis between SiC and W_2C, fewer misfit dislocations need to be created to relax the stress in W_2C, it is more favorable.

The Si-C-W ternary phase diagram indicates that moving along the W-SiC line, if hcp W_2C is formed, one should have a simultaneous formation of tungsten silicides (W_6Si_3). Comparing binary diagram of tungsten carbide and silicide, it appears that melting temperatures of silicides are much lower than carbides which may explain the observed increased mobility at the interface. Note that the bulk self-diffusion of W at the interface cannot explain the observed dewetting kinetics. At 1900 °C, the self-diffusion coefficient of W is typically below 1×10^{-14} $cm^2.s^{-1}$ [37]. Assuming of diffusion type motion, 10000 s would be required to form the 100 nm-wide nodules, which is much longer than the 1800 s of annealing we did. Hence, it appears that alloying strongly increase the kinetics of diffusion of W in the confined SiC interface.

A transition from a continuous layer to inclusions was also reported in SiC/Si/SiC structures [12]. The existence of a similar phenomenon in SiC/W/SiC structure suggests a significant dewetting of tungsten from SiC surfaces, likely driven by the reduction of interfacial energies. To the best of our knowledge, the dewetting of W thin films from SiC substrates and a W/SiC contact angle have not been reported so. From our observations, we can suggest a large (>90°) W/SiC contact angle and a high interface energy resulting in a favored dewettting at the interfaces. There are very few mechanisms for matter transport. It seems that alloying strongly increase the diffusion of W at the interface. When a new W:Si:C alloy is formed, the binding energy of W, Si and C is changed. The melting point of tungsten carbide and tungsten silicide decreases drastically compared to pure W. As a result, the binding energy of W in these alloys becomes smaller, the activation energy for diffusion of W atoms decreases and the diffusion coefficient increases, enabling the film fragmentation.

The electrical resistivity of the W_2C phase is low, around 75.7 μΩ.cm [31] which makes its presence at the interface favorable for a good conduction. The contact resistance between W_2C and 4H-SiC is estimated of $1.7.10^{-3}$ Ω.cm^2 [38]. The direct 4H-SiC/3C-SiC/4H-SiC interface around the nodules also satisfies the requirement for a good conductance. Voids and oxide layers are often the cause of poor conduction [6,39]. From our observations, no such objects are created at the interface and a good conduction can be expected. Thus, the use of tungsten for SiC/SiC bonding seems to be a valuable option for application in high power electronics.

For titanium bonding, we evidenced Ti redistribution and its chemical reactions with Si and C atoms, rather than its dewetting from the SiC substrates. No evident fragmentation of Ti film is observed. On the other hand, Ti promotes SiC surfaces reconstruction by step bunching, an effect similar to that observed with W and Si layers [12] which requires also significant Ti transport. Step bunching mechanism is driven by the dissolution and recondensation of C and Si atoms at SiC internal surfaces. Small steps transform into high steps and wide terraces to create low-index facets that are energetically more favorable. Similar to W layers, Ti layers are transformed into new complex phases. The mechanisms of amplified SiC dissolution at SiC/Ti interfaces and amplified Ti, Si, C diffusion enable the evolution of interface morphology, step-bunching and the formation of carbides and silicides in spite of a still low solubility of carbon in titanium (≈3.1 at.%) [36]. Three different phases were identified after annealing: the Ti_3SiC_2 MAX phase has been formed in the thin layer, along with a cubic TiC phase above it. The thick nodules obey the structure of the $TiSi_2$ phase. We believe that the Ti layer becomes supersaturated with Si and C atoms upon dissolution of the SiC inner surfaces. Ti, Si and C atoms are then recondensated into thermodynamically favorable structures such as Ti_3SiC_2 and TiC [40], which also cost less elastic energy with regard to their in-plane misfit with SiC substrates. In the end, the remaining Ti layer is Si-rich due to a more pronounced recondensation of C atoms. The $TiSi_2$ phase is thus created during crystallization in the form of thick clusters. The formation of new crystalline phases may decrease the interfacial energy and the driving force for dewetting. Thus, we do not see any dewetting since all the internal surfaces are covered by the material. In good accordance with our experiments, dewetting of titanium thin films on SiC substrates has not been reported in the literature. The mechanisms involving the dissolution, transport, and recondensation of carbon and silicon atoms allowing SiC surfaces reconstruction are significantly favored at higher temperatures which results also in enhanced step bunching after annealing at 1700 °C.

The formation of Ti_3SiC_2 or TiC over SiC substrate has been well studied in the literature [41–48] and the authors mentioned a good ohmic contact with a contact resistivity of around 10^{-4}-10^{-5} Ω.cm^2. The formation of Ti_3SiC_2 and TiC improves the conduction at the interface between the two SiC substrates. Similarly to W, bonding with titanium thin film without creation of voids or oxide layers seems to be a good option to ensure a good adhesion between the two substrates and a good interfacial conductivity.

Investigations on Ni-Ti-Al ohmic contacts obtained on p-type 4H-Si.

Investigations on Ni-Ti-Al ohmic contacts obtained on p-type.

5. Conclusions

We studied the phase transformations occurring in the SiC/W/SiC and SiC/Ti/SiC structures under high temperature annealing. For the two materials, we evidence specific structural and compositional transformations in the layers and the internal SiC surfaces as a function of annealing temperature.

We demonstrated that an amorphous, homogeneous and continuous film created after deposition transforms into a discontinuous crystalline

structure for W layer and into continuous but phase separated and thickness variable structures for Ti layer, following high temperature annealing. All the structures reached an epitaxial relationship with the SiC substrates. We identified the transformation of the W layer into the W_2C phase, which was fully relaxed by the formation of misfit dislocations. The Ti layer is transformed into three phases, namely Ti_3SiC_2, TiC, $TiSi_2$ which are found mostly pseudomorphic to the SiC structure. As a result, they became in-plane tensile stressed. While enrichment of Ti with Si and C atoms ensured good wetting of the eventual layer on the SiC surfaces, W enrichment with C atoms strongly enhanced its dewetting. Such a finding suggests that Ti, Si and/or C alloys on SiC obey a relatively low interfacial energy, while W_2C/SiC phase has a high interfacial energy. The latter results in the creation of isolated nodules already for the temperatures below the melting point. It was accompanied by the creation of 4H-SiC/3C-SiC/4H-SiC contacts around the W_2C nodules.

The strong interface evolution of SiC internal surfaces by step bunching was evidenced. The presence of C and Si atoms within the new phases was provided by the dissolution of few (0004) SiC layers during annealing. Chemical reactions are a mechanism at work at the interface even at relatively low temperatures, below the melting points.

All the new phases formed from the W and Ti layers represent highly conductive materials. Thus, SiC to SiC bonding with these materials seems to be a promising approach to provide a good enough adhesion between the two SiC substrates and ensure a high conductivity of the interfaces, a necessary requirement for such substrate applications in power electronics.

CRediT authorship contribution statement

Maëlle Le Cunff: Writing – original draft, Methodology, Investigation, Formal analysis, Data curation. **François Rieutord:** Writing – review & editing, Methodology, Investigation, Formal analysis. **Didier Landru:** Writing – review & editing, Funding acquisition, Conceptualization. **Oleg Kononchuk:** Writing – review & editing, Conceptualization. **Nikolay Cherkashin:** Writing – review & editing, Writing – original draft, Supervision, Methodology, Investigation, Funding acquisition, Formal analysis, Conceptualization.

Declaration of competing interest

The authors declare that they have no known competing financial interests or personal relationships that could have appeared to influence the work reported in this paper.

Acknowledgements

Access to STEM facilities at the Raimond Castaing Microanalysis Centre, Toulouse and support of Teresa Hungria and Sébastien Joulié during experiments are gratefully acknowledged. Beamtime from French CRG BM32 beamline and support of beamline staff during synchrotron experiments is also acknowledged.

Data availability

Data will be made available on request.

References

[1] H. Abderrazak and E. S. Bel Hadj Hmida, Silicon Carbide: Synthesis and Properties, in: Properties and Application of Silicon Carbide, (2011). 10.5772/15736.
[2] Y.J. Shin, Study of a high temperature solution growth process for the development of heavily doped 4H-SiC substrates, Ph.d. Thesis (chemical and Process Engineering, Université Grenoble Alpes (2016).
[3] N. Daval, A. Drouin, H. Biard, L. Viravaux et al, SmartSiC™ for Manufacturing of SiC Power Devices, 6th IEEE Electron Devices Technology & Manufacturing Conference (EDTM), (2022) 85-87. 10.1109/EDTM53872.2022.9798032.
[4] S. Rouchier, G. Gaudin, J. Widiez, et al., 150 mm SiC Engineered Substrates for High-Voltage Power Devices, Mater. Sci. Forum 1062 (2022) 131–135, https://doi.org/10.4028/p-mxxdef.
[5] T. Boudet, Advanced substrates for power electronics, International VLSI Symposium on Technology, Systems and Applications (2023) 1–2, https://doi.org/10.1109/VLSI-TSA/VLSI-DAT57221.2023.10134040.
[6] P. Ivanov, L. Kostina, A. Potapov, T. Samsonova, E. Belyakova, T. Argunova, I. Grekhov, Current-voltage characteristics of isotype SiC-SiC junctions fabricated by direct wafer bonding, Semiconductors 41 (2007) 921–924, https://doi.org/10.1134/S1063782607080106.
[7] S. Hu, Y. Huang, T. Liu, J. Guo, A comparative study of a deep-trench superjunction SiC VDMOS device, J. Comput. Electron. 18 (2019) 553–560, https://doi.org/10.1007/s10825-019-01318-2.
[8] H. Moriceau, F. Rieutord, F. Fournel, Y. Le Tiec, L. Di Cioccio, C. Morales, A. M. Charvet, C. Deguet, Overview of recent direct wafer bonding advances and applications, Adv. Nat. Sci. Nanosci. Nanotechnol. 1 (043004) (2010), https://doi.org/10.1088/2043-6262/1/4/043004.
[9] O. Kononchuk, D. Landru, C. Veytizou, E. Guiot, Recent advances in the Smartcut™ technology for CMOS applications, ECS Trans. 33 (11) (2010) 23–34, https://doi.org/10.1149/1.3485680.
[10] A. Yi, Y. Zheng, H. Huang, J. Lin, Y. Yan, T. You, K. Huang, S. Zhang, C. Shen, M. Zhou, W. Huang, J. Zhang, S. Zhou, H. Ou, and X. Ou, Wafer-scale 4H-silicon carbide-on-insulator (4H-SiCOI) platform for nonlinear integrated optical devices, Optical Materials, 107(109990), (2020). 10.1016/j.optmat.2020.109990.
[11] F. Letertre, J. Brault, I. Matko, F. Enjalbert, E. Bellet-Amalric, G. Feuillet, C. Richtarch, B. Faure, L. DiCioccio, R. Madar, B. Daudin, E. Monroy, Smart Cut™ SiCOI wafers for MBE GaN epitaxy, Phys. Status Solidi 7 (2003) 2103–2106, https://doi.org/10.1002/pssc.200303306.
[12] M. Le Cunff, F. Rieutord, D. Landru, O. Kononchuk, N. Cherkashin, High temperature evolution of a confined silicon layer, J. Appl. Phys. 135 (245301) (2024), https://doi.org/10.1063/5.0205878.
[13] F. Triendl, G. Pfusterschmied, S. Schwarz, G. Pobegen, J.P. Konrath, U. Schmid, Barrier height tuning by inverse sputter etching at poly-Si/4H-SiC heterojunction diodes, Semicond. Sci. Technol. 36 (5) (2021) 055021, https://doi.org/10.1088/1361-6641/abf29b.
[14] T. Shimatsu, M. Uomoto, Atomic diffusion bonding of wafers with thin nanocrystalline metal films, J. Vac. Sci. Technol. B 28 (2010) 706–714, https://doi.org/10.1116/1.3437515.
[15] M. Uomoto and T. Shimatsu, Atomic diffusion bonding of Si wafers using Nb films, Japanese Journal of Applied Physics, 59(SBBC04), (2019). 10.7567/1347-4065/ab4b1c.
[16] T. Shimatsu, M. Uomoto, H. Kon, Room Temperature Bonding Using Thin Metal Films, ECS Trans. 64 (5) (2014) 317–328, https://doi.org/10.1149/06405.0317ecst.
[17] T. Shimatsu, M. Uomoto, Room Temperature Bonding of Wafers with Thin Nanocrystalline Metal Films, ECS Trans. 33 (2010) 61–72, https://doi.org/10.1149/1.3483494.
[18] Periodic Table Tungsten. https://www.rsc.org/periodic-table/element/74/tungsten.
[19] Periodic Table Titanium. https://www.rsc.org/periodic-table/element/22/titanium.
[20] N. Cherkashin, A. Louiset, A. Chmielewski, D.J. Kim, C. Dubourdieu, S. Schamm-Chardon, Quantitative mapping of strain and displacement fields over HR-TEM and HR-STEM images of crystals with reference to a virtual lattice, Ultramicroscopy 253 (113778) (2023), https://doi.org/10.1016/j.ultramic.2023.113778.
[21] E. Jette, F. Foote, Precision Determination of Lattice Constants, J. Chem. Phys. 3 (1935) 605–616, https://doi.org/10.1063/1.1749562.
[22] Yu.B. Kuz'ma, V.I. Lakh, V.Ya. Markiv, B.I. Stadnyk, E.I. Gladyshevskii, X-ray diffraction study of the system tungsten-rhenium-carbon, Powder Metall. Met. Ceram. 2 (1964) 286–292, https://doi.org/10.1007/BF00774034.
[23] N. Cherkashin, T. Denneulin, M. Hÿtch, Electron microscopy by specimen design: application to strain measurements, Sci. Rep. 7 (12394) (2017), https://doi.org/10.1038/s41598-017-12695-8.
[24] M. Sabeena, S. Murugesan, P. Anees, E. Mohandas, M. Vijayalakshmi, Crystal structure and bonding characteristics of transformation products of bcc β in Ti-Mo alloys, J. Alloy. Compd. 705 (2017) 769–781, https://doi.org/10.1016/j.jallcom.2016.12.155.
[25] C.J. Rawn, E.A. Payzant, C.R. Hubbard, M.W. Barsoum, T. El-Raghy, Structure of Ti_3SiC_2, Mater. Sci. Forum 321 (2000) 889–892, https://doi.org/10.4028/www.scientific.net/MSF.321-324.889.
[26] K. Nakamura, M. Yashima, Crystal structure of (NaCl)-type transition metal monocarbides MC (M=V, Ti, Nb, Ta, Hf, Zr), a neutron powder diffraction study, Mater. Sci. Eng., B 148 (2008) 69–72, https://doi.org/10.1016/j.mseb.2007.09.040.
[27] V.P. Kopylova, T.N. Nazarchuk, Determination of free metals and oxides in powdered disilicides of transition metals of groups IV-VI, Ind. Lab. 43 (1977) 485–487.
[28] T. Dash, B. Nayak, M. Abhangi, R. Makwana, S. Vala, S. Jakhar, C.V. Rao, T. K. Basu, Preparation and Neutronic Studies of Tungsten Carbide Composite, Fusion Sci. Technol. 65 (2014) 241–247, https://doi.org/10.13182/FST13-663.
[29] E.M. Garcia-Ayala, S. Tarancon, B. Ferrari, J.Y. Pastor, A.J. Sanchez-Herencia, Thermodynamical behaviour of WC-W2C composites at first wall in fusion conditions, Int. J. Refract Metal Hard Mater. 98 (2021) 105565, https://doi.org/10.1016/j.ijrmhm.2021.105565.

[30] L. Knoll, V. Teodorescu, A. Minamisawa, Ultra-thin Epitaxial Tungsten Carbide Schottky Contacts in 4H-SiC, IEEE Electron Device Lett. 37 (2016) 1318–1320, https://doi.org/10.1109/LED.2016.2604488.
[31] H. Taimatsu, S. Sugiyama, Y. Kodaira, Synthesis of W2C by Reactive Hot Pressing and Its Mechanical Properties, Mater. Trans. 49 (2008) 1256–1264, https://doi.org/10.2320/matertrans.MRA2007304.
[32] S. DelaCruz, Z. Wang, P. Cheng, C. Carraro, R. Maboudian, TiN diffusion barrier for stable W/SiC(0001) interfaces in inert ambient at high temperature, Thin Solid Films 670 (2019) 54–59, https://doi.org/10.1016/j.tsf.2018.11.058.
[33] H. Romanus, V. Cimalla, S. Ahmed, J.A. Schaefer, L. Spiess, G. Ecke, J. Pezoldt, Preparation of single phase tungsten carbide by annealing of sputtered tungsten-carbon layers, Thin Solid Films 359 (2000) 146–149, https://doi.org/10.1016/S0040-6090(99)00732-4.
[34] L. Baud, C. Jaussaud, R. Madar, C. Bernard, J.S. Chen, M.A. Nicolet, Interfacial reactions of W thin film on single crystal (001) β-SiC, Mater. Sci. Eng. B 29 (1995) 126–130, https://doi.org/10.1016/0921-5107(94)04017-X.
[35] T.T. Thabethe, T.T. Hlatshwayo, E.G. Njoroge, T.G. Nyawo, T.P. Ntsoane, J. B. Malherbe, Interfacial reactions and surface analysis of W thin film on 6H-SiC, Nucl. Inst. Methods Phys. Res. B 371 (2016) 235–239, https://doi.org/10.1016/j.nimb.2015.10.063.
[36] H.J. Goldschmidt, J.A. Brand, The tungsten-rich region of the system tungsten-carbon, J. Less Common Metals 5 (2) (1963) 181–184, https://doi.org/10.1016/0022-5088(63)90012-2.
[37] J.N. Mundy, S.J. Rothman, N.Q. Lam, L.J. Nowicki, H.A. Hoff, Self-diffusion in tungsten, J. Nucl. Mater. 69–70 (1978) 526–528, https://doi.org/10.1016/0022-3115(78)90264-7.
[38] H. Romanus, Siliziumkarbidelektronik - technologische und werkstoffwissenschaftliche untersuchungen zur metallisierung/kontaktierung, Ph. d Thesis (technishen Universität Ilmeneau (2003).
[39] L. Han, Y. Zou, B. Jia, X. Guan, H. Zhao, Y. Hu, X. Zhang, P. Lu, Atomic and electronic properties of different types of SiC/SiO2 interfaces: First-principles calculations, Surf. Interfaces 33 (2022) 102273, https://doi.org/10.1016/j.surfin.2022.102273.
[40] D. Bandyopadhyay, The Ti-Si-C system (Titanium,-Silicon-Carbon), J. Phase Equilib. Diffus. 25 (2004) 415–420, https://doi.org/10.1007/s11669-004-0132-7.
[41] F. Laariedh, M. Lazar, P. Cremillieu, J.L. Leclercq, Investigations on Ni-Ti-Al Ohmic Contacts Obtained on P-type 4H-SiC, Mater. Sci. Forum 711 (2012) 169–173, https://doi.org/10.4028/www.scientific.net/MSF.711.169.
[42] K. Buchholt, R. Ghandi, M. Domeij, C.M. Zetterling, J. Lu, P. Eklund, L. Hultman, A. Lloyd Spetz, Ohmic contact properties of magnetron sputtered Ti_3SiC_2 on n- and p-type 4H-silicon carbide, Appl. Phys. Lett. 98 (042108) (2011), https://doi.org/10.1063/1.3549198.
[43] B. Pécz, L. Toth, M.A. di Forte-Poisson, J. Vacas, Ti_3SiC_2 formed in annealed Al/Ti contacts to p-type SiC, Appl. Surf. Sci. 206 (2003) 8–11, https://doi.org/10.1016/S0169-4332(02)01195-9.
[44] T. Abi-Tannous, M. Soueidan, G. Ferro, M. Lazar, C. Raynaud, B. Toury, M. F. Beaufort, J.F. Barbot, O. Dezellus, D. Planson, A Study on the Temperature of Ohmic Contact to p-type SiC Based on Ti_3SiC_2 Phase, IEEE Trans. Electron Devices 63 (6) (2016) 1–7, https://doi.org/10.1109/TED.2016.2556725.
[45] A. Drevin-Bazin, J.F. Barbot, T. Cabioch, M.F. Beaufort, Investigations of Ti_3SiC_2 MAX phase formation onto N-type 4H-SiC, Mater. Sci. Forum 717 (2012) 845–848, https://doi.org/10.4028/www.scientific.net/MSF.717-720.845.
[46] H. Fashandi, M. Andersson, J. Eriksson, J. Lu, K. Smedfors, C.-M. Zetterling, A. Lloyd Spetz, P. Eklund, Single-step synthesis process of Ti_3SiC_2 ohmic contacts on 4H-SiC by sputter-deposition of Ti, Scr. Mater. 99 (2015) 53–56, https://doi.org/10.1016/j.scriptamat.2014.11.025.
[47] M. De Silva, T. Kawasaki, T. Miyazaki, T. Koganezawa, S. Yasuno, S.-I. Kuroki, Formation of epitaxial Ti-Si-C Ohmic contact on 4H-SiC C face using pulsed-laser annealing, Appl. Phys. Lett. 110 (252108) (2017), https://doi.org/10.1063/1.4987136.
[48] S.-K. Lee, C.-M. Zetterling, E. Danielsson, M. Ostling, J.-P. Palmquist, H. Hogberg, U. Jansson, Electrical characterization of TiC ohmic contacts to aluminium ion implanted 4H-silicon carbide, Appl. Phys. Lett. 77 (2000) 1478–1480, https://doi.org/10.1063/1.1290690.